

AperTO - Archivio Istituzionale Open Access dell'Università di Torino

Electron-density critical points analysis and catastrophe theory to forecast structure instability in periodic solids

This is the author's manuscript

Original Citation:

Availability:

This version is available <http://hdl.handle.net/2318/1660024> since 2018-02-16T11:28:36Z

Published version:

DOI:10.1107/S2053273317018381

Terms of use:

Open Access

Anyone can freely access the full text of works made available as "Open Access". Works made available under a Creative Commons license can be used according to the terms and conditions of said license. Use of all other works requires consent of the right holder (author or publisher) if not exempted from copyright protection by the applicable law.

(Article begins on next page)

Electron-density critical points analysis and catastrophe theory to forecast structure instability in periodic solids

Marcello Merli^{a*} and Alessandro Pavese^b

Received 21 November 2017

Accepted 22 December 2017

Edited by W. F. Kuhs, Georg-August University Göttingen, Germany

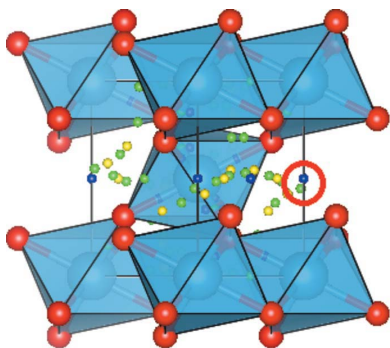
Keywords: electron-density critical points; catastrophe theory; phase/state transitions in crystals; *ab initio* calculations.

^aEarth and Sea Sciences Department (DiSTeM), University of Palermo, Via Archirafi 36, Palermo, 90126, Italy, and ^bEarth Sciences Department, University of Turin, Via Valperga Caluso 35, Turin, 10100, Italy. *Correspondence e-mail: marcello.merli@unipa.it

The critical points analysis of electron density, *i.e.* $\rho(\mathbf{x})$, from *ab initio* calculations is used in combination with the catastrophe theory to show a correlation between $\rho(\mathbf{x})$ topology and the appearance of instability that may lead to transformations of crystal structures, as a function of pressure/temperature. In particular, this study focuses on the evolution of coalescing non-degenerate critical points, *i.e.* such that $\nabla\rho(\mathbf{x}_c) = 0$ and $\lambda_1, \lambda_2, \lambda_3 \neq 0$ [λ being the eigenvalues of the Hessian of $\rho(\mathbf{x})$ at \mathbf{x}_c], towards degenerate critical points, *i.e.* $\nabla\rho(\mathbf{x}_c) = 0$ and at least one λ equal to zero. The catastrophe theory formalism provides a mathematical tool to model $\rho(\mathbf{x})$ in the neighbourhood of \mathbf{x}_c and allows one to rationalize the occurrence of instability in terms of electron-density topology and Gibbs energy. The phase/state transitions that TiO_2 (rutile structure), MgO (periclase structure) and Al_2O_3 (corundum structure) undergo because of pressure and/or temperature are here discussed. An agreement of 3–5% is observed between the theoretical model and experimental pressure/temperature of transformation.

1. Introduction

Impressive advances have been achieved in reconstructing the electron density, $\rho(\mathbf{x})$, of periodic solids at non-ambient conditions from experimental data. Macchi & Casati (2011), Fabbiani *et al.* (2011) and Yamanaka *et al.* (2009) have pioneered high-pressure electron-density determination by diffraction experiments, using multipolar analysis or the maximum entropy method. Casati *et al.* (2016, 2017) have definitely proved the possibility of reconstructing experimental electron density even at high pressure, by exploiting a combination of techniques [multipolar analysis, ELMOs (energy-localized molecular orbitals), XC-ELMO-VB (X-ray constrained ELMO valence bond)] and opening a new perspective upon the role $\rho(\mathbf{x})$ may play in shedding light on transformations at non-ambient conditions. Dittrich (2017) and Macchi (2017) critically discuss the potential role electron-density topology may have in future to disclose novel paths for interpretation and/or prediction of a variety of phenomenologies in molecules and periodic solids. Andrés *et al.* (2015) stress the role of electron-density topology in obtaining insight into reaction mechanisms, which imply a loss of equilibrium for a transformation to take place. Tse *et al.* (2006), Contreras-García, Martín Pendás, Silvi *et al.* (2008) and Contreras-García, Martín Pendás & Recio (2008) point out how external perturbation, like pressure, change electron density in such a way as to induce important modifications of the physical properties of a crystal. In keeping with the DFT (density functional theory) formulation, all this underlines the



© 2018 International Union of Crystallography

paramount part that $\rho(\mathbf{x})$ topology plays in relation to periodic solid behaviour in non-ambient regimes. Therefore, it becomes natural to focus one's attention on the correlations between electron-density properties and the occurrence of instability in a periodic phase as a function of pressure (P) and/or temperature (T).

In general, tokens of instability are crucial to steer research aimed at exploration of the transformations crystals undergo at non-ambient conditions. In the case of minerals, although it is possible, nowadays, to achieve extreme conditions in the laboratory mimicking planetary interiors (Miletich, 2005; Hemley, 1998), the measurements are still carried out far from thermodynamic equilibrium and with relevant experimental difficulties, which are a serious hindrance to getting insights into details of the investigated phases and understanding the driving mechanisms. The occurrence of intermediate metastable phases in certain crystal solid-state transitions and the intrinsic complexity of the phenomena involved (Boldyreva & Dera, 2009) require rigorous theoretical support, particularly with regard to those mechanisms that make instability rise (Catti, 2002, 2005).

Being able to detect the appearance of signals that portend instability and thereby lead to possible subsequent transformations of crystals provides a valuable auxiliary tool to non-ambient conditions studies (Ghose *et al.*, 2012). From a microscopic point of view, soft modes have long been used to predict changes in crystal phases (Fleury, 1976; Scott, 1974).

Electron density, in turn, is a natural candidate to forecast the approach of a transition/transformation that implies bonding and structure rearrangements (Bader, 1990) in crystals. Any transformation that requires a structure change of the parent phase must be preceded by the appearance of instability, which can be considered a prologue to a catastrophe then leading to a new disposition of atoms so as to achieve a stable configuration at given conditions. All this points to a growing attention on electron density as an observable that can in principle provide signals related to transformation of a crystal structure to a more stable configuration.

A contribution to achieving such a goal may be provided by combining electron-density topology analysis with theoretical techniques developed by the 'catastrophe theory' (Thom, 1975). The latter is a theoretical tool of applied mathematics, originally developed to predict the behaviour of dynamic systems, in which small variations of some parameters of theirs can cause abrupt changes in terms of equilibrium. Pioneering works that couple Bader's topological analysis and Thom's catastrophe theory of inorganic crystal structures are found in Luaña *et al.* (1997), Pendás *et al.* (1997), Merli *et al.* (2011), Parisi *et al.* (2012) and Merli & Sciascia (2013).

In the present work we aim (i) to shed light on the theoretical links between crystal electron-density topology at critical points, energetics, catastrophe theory formalism and the appearance of instability in periodic solids; (ii) to discuss some case studies in which we practically use the notions from (i) and compare the occurrence of instability signals, which allows us to predict the collapse of the erstwhile crystal

structure, with experimentally determined pressure/temperature values of transition. In particular, we pay attention to the high-temperature melting of TiO_2 (rutile structure), high-pressure phase transition of Al_2O_3 (corundum structure), high-temperature melting of MgO (periclase structure), high-pressure and high-temperature phase transition of MgO (periclase). The electron density is determined by static quantum mechanical calculations and then rendered dynamic to account for atomic thermal motion.

2. Theoretical background

2.1. Critical points

Let $\rho(\mathbf{x})_X$ be the electron density of a crystal at a given X value of an intensive thermodynamic variable, such as pressure or temperature. \mathbf{x}_0 locates a critical point, *i.e.* $\nabla_{\mathbf{x}}\rho(\mathbf{x}_0)_X = 0$. If one expands $\rho(\mathbf{x})_X$ around \mathbf{x}_0 , then

$$\rho(\mathbf{x})_X \simeq \rho(\mathbf{x}_0)_X + \frac{1}{2} H_{ji}(\mathbf{x}_0)_X \Delta x_j \Delta x_i + O(\Delta x^3) \quad (1)$$

where $\Delta x_i = x_i - x_{0i}$ and $H_{ji}(\mathbf{x}_0)_X = (\partial^2 \rho) / (\partial x_j \partial x_i)_{0,X}$, *i.e.* the Hessian matrix of $\rho(\mathbf{x})_X$ at \mathbf{x}_0 . \mathbf{x}_0 , in turn, is a function of X . Given that $H_{ji}(\mathbf{x}_0)_X = H_{ij}(\mathbf{x}_0)_X$, then it has real eigenvalues, $\lambda(X)_j$, and can be turned into a diagonal matrix by a linear change of coordinates. For the sake of simplicity, let us assume that the \mathbf{x} coordinates already are those that diagonalize the Hessian matrix, so that equation (1) changes into

$$\rho(\mathbf{x})_X \simeq \rho(\mathbf{x}_0)_X + \frac{1}{2} \sum_{j=1,3} \lambda_j(X) \times \Delta x_j^2 + O(\Delta x^3). \quad (2)$$

If $\det[\mathbf{H}(\mathbf{x}_0)_X] \neq 0$, then $\lambda_j(X) \neq 0$ for $j = 1-3$, and \mathbf{x}_0 is called a *non-degenerate* critical point. Each critical point, hereafter CP, has associated a symbol, *i.e.* (ω, σ) , where ω and σ are *rank* and *signature* of $\mathbf{H}(\mathbf{x}_0)$, respectively. The former represents the number of eigenvalues other than zero; the latter is the result of the algebraic sum of the eigenvalues' signs.

If $\det[\mathbf{H}(\mathbf{x}_0)_{Xc}] = 0$ for a given Xc value of X , then at least one eigenvalue is null, *i.e.* $\ker[\mathbf{H}(\mathbf{x}_0)_{Xc}]$ does not coincide with the null vector, and \mathbf{x}_0 is a *degenerate* critical point. Degenerate CPs of a generic function F are the key to developing any application of Thom's catastrophe theory, as they can be the origin of local abrupt changes of F , this all leading to instability conditions. Let us assume, for the sake of simplicity, that $\lambda_1(Xc) = 0$ and $\lambda_1(Xc \pm \delta X) \neq 0$. In such a case, equation (2) is then expandable at $X = Xc$ around \mathbf{x}_0 as

$$\rho(\mathbf{x})_{Xc} \simeq \rho(\mathbf{x}_0)_{Xc} + \frac{1}{2} [\lambda_2(Xc) \times \Delta x_2^2 + \lambda_3(Xc) \times \Delta x_3^2] + \Phi(\Delta x_1)_{Xc}. \quad (3)$$

$\Phi(\Delta x_1)_{Xc}$ is a function that can be described by the splitting theorem of Thom, so that

$$\Phi(\Delta x_1)_{Xc} = \text{CG}(\Delta x_1) + \text{Pert}(\Delta x_1)$$

where CG and Pert are 'Catastrophe Germ' and 'Perturbation', respectively. In particular

$$\text{CG}(\Delta x_1) = \alpha_{k+1} \times (\Delta x_1)^{k+1} \quad (4a)$$

$$\text{Pert}(\Delta x_1) = \sum_{j=1, k=1} \alpha_j \times (\Delta x_1)^j, \quad (4b)$$

where $\{\alpha\}$ is a set of parameters, known as ‘control parameters’ (Arnol’d, 1986), with $\alpha_{k+1} \neq 0$ and $k \geq 2$ (Gilmore, 1993). The combination of equations (4a) and (4b) gives the ‘unfolding catastrophe function’. For the sake of completeness, there exists a smooth change of coordinates, *i.e.* $\Delta x_1 \rightarrow y$, which turns CG + Pert into y^{k+1} , *i.e.* a ‘Germ’-like function that bears the very ‘essence’ of the catastrophe expansion.

$\Phi(\Delta x_1)_{Xc}$ is the origin of anomalies, given that even very small changes of its control parameters can deeply affect the nature of the function and of the $\rho(\mathbf{x})$ ’s local topology along the Hessian eigenvector $\boldsymbol{\varepsilon}_1$ as a consequence. For instance, structure fluctuations due to thermal agitation or distortions due to pressure cause, at degenerate CPs, a topological change which corresponds to a re-arrangement of bonding (Bader, 1990; Matta & Boyd, 2007) and heralds a possible re-adjustment of atoms towards a more stable configuration.

This aspect can be understood analysing the behaviour of a generic function depending on \mathbf{x} and on a set of control parameters, *i.e.* $\Xi(\mathbf{x}, \{\alpha\})$, and such that $\nabla \Xi(\mathbf{x}_c, \{\alpha_c\}) = 0$. If $\{\alpha'_c\} = \{\alpha_c\} + \{\delta\alpha_c\}$, then we expect that $\mathbf{x}'_c = \mathbf{x}_c + \delta\mathbf{x}_c$. It is trivial to demonstrate that if Ξ is *non*-degenerate at $(\mathbf{x}_c, \{\alpha_c\})$, then $\delta\mathbf{x}_c$ is expressible as a linear combination of $\{\delta\alpha_c\}$, *i.e.* a CP smoothly changes its position as a function of the control parameters and $\delta\mathbf{x}_c$ is univocally determined. A failure of ‘unicity’ of the $\delta\mathbf{x}_c$ ’s solution as a function of $\{\delta\alpha_c\}$ changes portends, in our case, an anomaly that can be associated with an incipient transformation (Gilmore, 1993; Sanns, 2009). For instance, a multi-furcation of CPs may take place, leading to possible degeneracy of CP, as discussed in §2.3 below.

2.2. Gibbs energy and critical points

The possible topological anomaly at CPs of electron density depends upon a solid’s Gibbs energy, which is a functional of $\rho(\mathbf{x})_X$, *i.e.* $G[\rho(\mathbf{x})_X]$. We split the functional integration over a three-dimensional region into two ranges; one is a sphere of radius r around \mathbf{x}_0 , *i.e.* Ω ; the other is the complementary volume other than Ω , *i.e.* $V - \Omega$. In so doing, we can write

$$\begin{aligned} G[\rho(\mathbf{x})_X] &= \int_0^V g[\rho(\mathbf{x})_X] dV = \int_\Omega g[\rho(\mathbf{x})_X] dV + \int_0^\Omega g[\rho(\mathbf{x})_X] dV \\ &= G_{X, V-\Omega} + G_{X, \Omega}. \end{aligned}$$

In the following we focus on the second term of the equation above, *i.e.* $G_{X, \Omega}$, which is the one significant to our purpose. Choosing r small enough and taking into account that $\lambda_1(Xc) = 0$ at $X = Xc$, the expression reported below holds:

$$\begin{aligned} G_{Xc, \Omega} &= \int_0^\Omega g[\rho(\mathbf{x}_0)_{Xc} + \frac{1}{2}[\lambda_2(Xc) \times \Delta x_2^2 + \lambda_3(Xc) \times \Delta x_3^2] \\ &\quad + \Phi(\Delta x_1)_{Xc}] dV. \end{aligned}$$

In the neighbourhood of \mathbf{x}_0 we split electron density as $\rho(\mathbf{x}) = \rho(\mathbf{x}_0) + \delta\rho(\mathbf{x})$, *i.e.* a modulation around a reference value.

Taking into account equation (3), a few algebraic manipulations lead to the following expansion:

$$\begin{aligned} G_{Xc, \Omega} &\simeq G[\rho(\mathbf{x}_0)_{Xc}] + \left(\frac{\partial g}{\partial \rho}\right)_{\rho(\mathbf{x}_0)_{Xc}} \\ &\quad \times \int_0^\Omega \left\{ \frac{1}{2}[\lambda_2(Xc) \times \Delta x_2^2 + \lambda_3(Xc) \times \Delta x_3^2] + \Phi(\Delta x_1)_{Xc} \right\} dV \\ &= A_0 + \left(\frac{\partial g}{\partial \rho}\right)_{\rho(\mathbf{x}_0)_{Xc}} [\lambda_2(Xc) \times A_2 + \lambda_3(Xc) \times A_3 \\ &\quad + \sum_{j=1, k+1; j \neq k} \alpha_j \times B_j] \end{aligned} \quad (5a)$$

where

$$A_0 = \frac{4}{3}\pi r^3 g[\rho(\mathbf{x}_0)_{Xc}], \quad (5b)$$

$$A_{2,3} = \int_0^\Omega \Delta x_{2,3}^2 dV = \frac{8}{15}\pi r^5, \quad (5c)$$

$$B_j = \int_0^\Omega \Delta x_1^j dV = \begin{cases} 16\pi/[(j+1)(j+3)]r^{j+3}, & j = 2m; j \neq k \\ 0, & j = 2m+1; j \neq k. \end{cases} \quad (5d)$$

One splits equation (5a) into

$$G_{Xc, \Omega} = G_{Xc, \Omega, \text{reg}} + G_{Xc, \Omega, \text{cat}}$$

where

$$G_{Xc, \Omega, \text{reg}} = r^3 \left\{ \frac{4}{3}\pi g[\rho(\mathbf{x}_0)_{Xc}] + \left(\frac{\partial g}{\partial \rho}\right)_{\rho(\mathbf{x}_0)_{Xc}} \frac{8}{15}\pi [\lambda_2(Xc) + \lambda_3(Xc)] r^2 \right\}$$

and

$$G_{Xc, \Omega, \text{cat}} = \left(\frac{\partial g}{\partial \rho}\right)_{\rho(\mathbf{x}_0)_{Xc}} \sum_{j=1, k+1; j \neq k} \alpha_j \tau_j \frac{16\pi}{[(j+1)(j+3)]r^{j+3}}. \quad (6)$$

$G_{Xc, \Omega, \text{reg}}$ represents the ‘regular’ contribution to the Gibbs energy, governed by the eigenvalues other than zero, whereas $G_{Xc, \Omega, \text{cat}}$ is the term depending on the catastrophe function and associated with the ρ -Hessian eigenvalue that becomes null. Given that

$$\tau_j = 1 \quad j = 2m, \quad \tau_j = 0 \quad j = 2m+1,$$

as the integration over Ω of an odd function like Δx_1^{2n+1} is null, only even terms in Δx_1 contribute to equation (5d). In the light of this, Φ , *i.e.* the catastrophe part of the electron density as defined in the previous section, can be split into two contributions:

$$\Phi(\Delta x_1)_{Xc} = \Phi_e(\Delta x_1)_{Xc} + \Phi_o(\Delta x_1)_{Xc}$$

where the subscripts ‘e’ and ‘o’ indicate the even and odd components of Φ , respectively, and the former only influences $G_{Xc, \Omega, \text{cat}}$.

The mechanism of instability induced by $G_{Xc, \Omega, \text{cat}}$ is apparent if one expands the $\Phi_e(\Delta x_1)_{Xc}$ function up to the sixth order. From equation (6), one has

$$G_{Xc,\Omega,\text{cat}} \propto r^9 + U \times r^7 + V \times r^5 \quad (7a)$$

and the related catastrophe manifold, *i.e.* (r, U, V) , is defined by

$$\frac{\partial G_{Xc,\Omega,\text{cat}}}{\partial r} = 0; \quad \frac{\partial^2 G_{Xc,\Omega,\text{cat}}}{\partial r^2} = 0.$$

In so doing, we trivially obtain the following parametrization fulfilling the constraints above:

$$r = r_0, \quad U = -18/7r_0^2, \quad (7b)$$

$$V = 9/5r_0^4. \quad (7c)$$

In Fig. 1 we show the U – V catastrophe manifold parametrized as a function of r_0 (‘integration critical radius’) such that if $r = r_0$ then the catastrophe conditions occur. Small changes of U – V around the catastrophe manifold can cause large variations of $G_{Xc,\Omega,\text{cat}}$. The condition producing a physical r_0 value is that $V > 0$ and $U < 0$. If such a condition fails to occur, then higher-order expansions should be used in place of (7a), so as to bring to light the connection between Gibbs energy, catastrophe occurrence and degeneracy of a CP. In practical cases, U and V may correlate with one another and with the other coefficients. This makes it difficult to determine precisely their signs, which may possibly exchange. In the light of this, it is preferable to use their ratio, *i.e.* $-V/U$, to determine r_0 , and hence the condition to be met in applications is $-V/U > 0$.

2.3. Coalescing CPs

The appearance of a degenerate CP is often associated with CP coalescence. Let us assume a and b to be CPs at \mathbf{x}_a and \mathbf{x}_b that tend to be near one another, as a function of X that approaches Xc . Note that $\det[\mathbf{H}(\mathbf{x}_a)_X] = \lambda_{1,a}(X)\lambda_{2,a}(X)\lambda_{3,a}(X)$ and $\det[\mathbf{H}(\mathbf{x}_b)_X] = \lambda_{1,b}(X)\lambda_{2,b}(X)\lambda_{3,b}(X)$. Let us also suppose that a and b coalesce at some Xc resulting in a CP, c , whose signature, at $X = Xc + \delta X$, is other than at least one of the coalescing points. In general, we observe that $\det[\mathbf{H}(\mathbf{x}_k)_X]$ behaves as a continuous function of X , owing to the continuity of the Hessian matrix terms. From this viewpoint, let us take, for instance, $\det[\mathbf{H}(\mathbf{x}_a)_{Xc-\delta X}] > 0$ and $\det[\mathbf{H}(\mathbf{x}_c)_{Xc+\delta X}] < 0$. As a regularly converges onto c and we can assume continuity of

$\det[\mathbf{H}(\mathbf{x}_a)_{Xc-\delta X}]$ and $\det[\mathbf{H}(\mathbf{x}_c)_{Xc+\delta X}]$ at Xc , then $\lim_{X \rightarrow Xc+} \det[\mathbf{H}(\mathbf{x}_c)_X] = \lim_{X \rightarrow Xc-} \det[\mathbf{H}(\mathbf{x}_a)_X] = 0$. This implies that at least one eigenvalue at $X = Xc$ of c/a must be equal to zero. Therefore, once a coalescing pair has been detected, one has to pay attention to the signature of the resulting CP and follow the evolution of the CP changing its signature. This is a practical and easy way to monitor the rise of instability conditions, expressed by annihilation of at least one eigenvalue and associated with coalescence between CPs. A similar reasoning implies that even an eigenvalue of b must become null at Xc .

Another case of interest is given by two CPs that have different signatures and coalesce into a non-critical point, *i.e.* a ‘wandering point’. For a and b we assume reasonably that

$$\lim_{X \rightarrow Xc-} \det[\mathbf{H}(\mathbf{x}_a)_X] = \lim_{X \rightarrow Xc-} \det[\mathbf{H}(\mathbf{x}_b)_X]$$

holds. Taking into account that, for instance, $\det[\mathbf{H}(\mathbf{x}_a)_X] > 0$ and $\det[\mathbf{H}(\mathbf{x}_b)_X] < 0$ for $X = Xc - \delta X$, it straightforwardly follows that $\lim_{X \rightarrow Xc-} \det[\mathbf{H}(\mathbf{x}_a)_X] = \lim_{X \rightarrow Xc-} \det[\mathbf{H}(\mathbf{x}_b)_X] = 0$. A similar argument can be used to state that $\lim_{X \rightarrow Xc-} \nabla \rho(\mathbf{x}_a)_X = \lim_{X \rightarrow Xc-} \nabla \rho(\mathbf{x}_b)_X = 0$. Altogether, for X tending to Xc , a and b coalesce into a degenerate CP, which then disappears into a wandering point, for $X = Xc + \delta X$.

2.4. Computational details and dynamic electron density

We have carried out static calculations and structure relaxations at given nominal pressure using the program *HF/DFT-CRYSTAL14* (Dovesi *et al.*, 2009), which implements ‘*Ab initio* Linear-Combination-of-Atomic Orbitals’ in the case of periodic systems. A Hamiltonian based on the WC1LYP functional (Scanavino *et al.*, 2012; Wu & Cohen, 2006) has been used in the present work, with a HF/DFT (HF = Hartree–Fock) hybridization ratio of 16%. The following values have been adopted for the tolerances governing the accuracy of the integrals of the self-consistent field (SCF) cycles: 10^{-9} for Coulomb overlap, 10^{-9} for Coulomb penetration, 10^{-9} for exchange overlap, 10^{-9} for exchange pseudo-overlap in direct space and 10^{-18} for exchange pseudo-overlap in reciprocal space, 10^{-10} a.u. (atomic units) threshold for SCF cycle convergence, shrinking factor of reciprocal space = 12 (Monkhorst net), shrinking factor of secondary reciprocal-space net = 24 (Gilat net). The Mg basis set from Causà *et al.* (1986) has been extended by the addition of diffuse *sp* and *d* shells (85-11G* contraction). The O basis set (6-31d1) of Gatti *et al.* (1994) has been used in the high-pressure simulations for all the investigated cases. The triple-zeta valence basis set augmented by one set of polarization functions (pob-TZVP; Peintinger *et al.*, 2013) has been chosen to model oxygen at high-temperature conditions for both periclase and rutile. The 86-411(d31)G basis set from Bredow *et al.* (2004) has been used for Ti. Al, in corundum, has been modelled by the 86-21G* basis set from Montanari *et al.* (2006). Further details on the *ab initio* computational setup can be found in Merli *et al.* (2011).

Atomic thermal motion and lattice parameter expansion at high-temperature conditions have been modelled using the

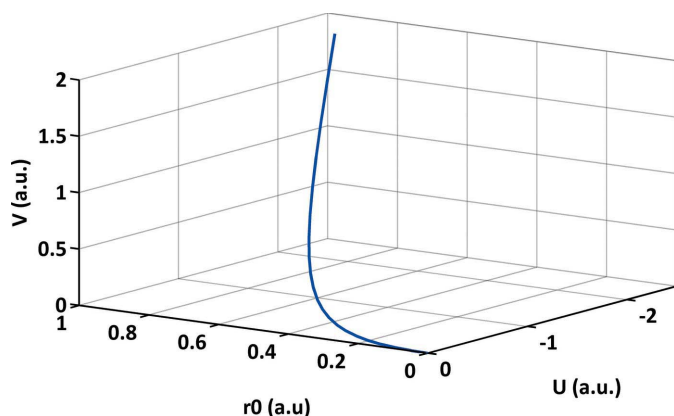


Figure 1

$G_{Xc,\Omega,\text{cat}}$ catastrophe manifold representation, through V and U as a function of r_0 . See equations (7b), (7c).

Table 1

Summary of the phase transitions/transformations investigated and classified according to the catastrophe theory formalism.

P in GPa and T in K. Elementary catastrophe functions of Thom, which are compatible with a given instability: fold, *i.e.* $a_1 \times x^3 + a_2 \times x$; cusp, *i.e.* $a_1 \times x^4 + a_2 \times x^2 + a_3 \times x$. RP = room pressure; RT = room temperature. References as follows: MgO (periclase melting) Dubrovinsky & Saxena (1997); MgO (B1→B2) McWilliams *et al.* (2012); TiO₂ (rutile melting) Guisbiers *et al.* (2008); Al₂O₃ (corundum→ Rh₂O₃ structure) Kato *et al.* (2013); SiO₂ (α-quartz→coesite) Merli & Sciascia (2013), Bose & Ganguly (1995); Mg₂Si₂O₆ (enstatite $Pbca$ → $Pbcn$) Merli *et al.* (2011). Investigations carried out by Merli & Sciascia (2013) and Merli *et al.* (2011) are reported here for completeness. NO, not observable.

	P, T observed	P, T predicted	CP transformations†	Elementary catastrophe function type	$\rho(\mathbf{x})$ type S: static D: dynamic
MgO (periclase melting)	RP and 3000 K	NO	(3,+1)+(3,-1)→ (3,+1)	Cusp	S D
MgO (B1→B2)	≈ 400 GPa and 9000 K	RP and 3100 K NO 500 GPa and 8650 K	(3,+1)+(3,-1)→ (3,+1)	Cusp	S D
TiO ₂ (rutile melting)	RP and ≈ 2143 K	RP and 4000 K RP and 2050 K	(3,+1)+(3,-1)→ (3,+1)	Cusp	S D
Al ₂ O ₃ (corundum→ Rh ₂ O ₃ structure)	≈120 GPa and RT ≈100 GPa and ≈2500 K ≈106 GPa and ≈1800 K	100 GPa 105 GPa and 1900 K	(3,+1)+(3,-1)→ (3,-1)	Cusp	S D
SiO ₂ (α-quartz→coesite)	≈2.7–3.2 GPa and 773–1273 K	≈ 4 GPa	(3,-1)+(3,1)→ WP	Fold	S
Mg ₂ Si ₂ O ₆ (enstatite $Pbca$ → $Pbcn$)	RP and 1360 K	≈ 1200 – 1400 K	(3,-1)+(3,1)→ WP	Fold	S

† CP transformations: $(X_a, Y_a) + (X_b, Y_b) \rightarrow (W, Z)$ means that two (X, Y) -type CPs coalesce into either one (W, Z) CP or one ‘wandering point’, *i.e.* WP. This implies one of the Hessian eigenvalues becomes 0 at given P and T .

following strategy. The structure has first been equilibrated at room pressure to determine a reference volume, *i.e.* $V(T_0)$. Then, using experimental thermal expansion, α , the volume has been changed to the values predicted accordingly, *i.e.* $V(T)$, and the structure has successively been relaxed at that fixed volume. If high pressure is also involved, we have equilibrated the structure at given P , neglecting the thermal contribution to the atomic relaxation. The effects of the atomic vibrations have been taken into account by rendering $\rho(\mathbf{x})_{\text{static}}$ dynamic. This has been accomplished by introducing anisotropic atomic displacement parameters (ADPs), determined at T , and thereby reconstructing $\rho(\mathbf{x})_{\text{dynamic}}$ by means of its dynamic Fourier coefficients, $F(T)_{hkl}$. $F(T)_{hkl}$'s, in turn, have been determined as the Fourier coefficients of the folding between the static electron density and the atomic probability distribution function (Merli *et al.*, 2002). The atomic displacement parameters have been estimated in two ways: (i) in the case of state transitions involving high temperature only, we have used extrapolations of experimental ADPs from experiments at comparable thermal conditions; (ii) in the case of transformations occurring in the regime of high pressure, we have calculated ADPs by lattice dynamics. Such a strategy is motivated by the fact that harmonic approximation gives largely underestimated ADPs, upon approaching a transition of state in the regime of high temperature and room pressure. By means of $F(T)_{hkl}$'s, determined up to $|\mathbf{H}| \approx 18 \text{ \AA}^{-1}$, we have reconstructed $\rho(\mathbf{x})_{\text{dynamic}}$ following two techniques: (i) inverse Fourier series and (ii) the maximum entropy method (MEM) (Merli *et al.*, 2002, 2009; Merli & Pavese, 2006). MEM calculations have been carried out by use of the code *BayMEM* (Van Smaalen *et al.*, 2003).

Extrapolation of experimental ADPs to a given temperature is a particularly delicate aspect. A δB change of the ADPs (here, for simplicity of notation, we assume an overall B

factor) affects the resulting dynamic electron density in terms of

$$\delta\rho \approx \frac{1}{V} \sum_{\mathbf{H}=-\infty}^{+\infty} -\frac{\mathbf{H}^2}{4} S_{\mathbf{H}} F_{\mathbf{H}} \exp(-2\pi i \mathbf{x} \mathbf{H}) \delta B$$

where $S_{\mathbf{H}}$ and $F_{\mathbf{H}}$ are the Fourier coefficients of the atomic probability distribution function and the static electron density, respectively. The expression above allows one to readily evaluate $\delta\rho/\delta T$, which is proportional to the ADPs' first derivatives *versus* temperature. We have used such an equation to check the sensitivity of $\rho(\mathbf{x})$ upon changing ADPs, paying special attention to verify that small B variations ascribable to experimental uncertainties do not alter the CP topology. Reverse Fourier and MEM reconstruction have provided fully consistent results, save that the former has failed in the case of TiO₂ to yield an electron density fulfilling the Hopf–Poincaré relation, *i.e.* $n_{(3,3)} - n_{(3,-1)} + n_{(3,+1)} - n_{(3,-3)} = 0$ (n_X means number of X -type CPs in the elementary cell). We think this is reflective of a numerical noise still present, notwithstanding a very large number of Fourier terms, which makes it difficult to discriminate low-electron-density CPs from fake CPs due to ripples. Yet, both methods have proven able to correctly recognize those CPs that are involved in the present study. In the light of the discussion above, we have chosen to use the results from the MEM filter. Pixels have been used to discretize each elementary cell, so as to fulfil the Nyquist–Shannon sampling condition and provide a resolution of $\sim 0.01 \text{ \AA}$. The topological analysis of the dynamic electron density has been carried out by means of the code *EDMA* contained in the *BayMEM* suite. Interpolation to calculate $\rho(\mathbf{x})$ out of the grid points has been carried out by means of the code *CRITIC2* (Otero-de-la-Roza *et al.*, 2009, 2014).

3. Results and discussion

We have investigated some phase/state transitions involving crystal structures of wide interest to many disciplines, to correlate the occurrence of instability to the $\rho(\mathbf{x})$ -CP behaviour, in the light of the discussion in the previous section. In Table 1 we summarize our results. The theoretical electron densities have been obtained from the wavefunctions calculated by *CRYSTAL14* for each structure, and the Bader's topological analysis has been performed by means of the module *TOPOND* (Gatti & Casassa, 2014) implemented therein.

3.1. MgO periclase melting at room pressure

MgO periclase has NaCl-type structure with Mg in octahedral coordination (space group $Fm\bar{3}m$; Hazen, 1976). Dubrovinsky & Saxena (1997) found the MgO melting point at room pressure and 3098(\pm 42) K. We have simulated the MgO periclase structure in a range from 300 up to 4000 K, using lattice parameters extrapolated from the experimental data of Reeber *et al.* (1995). Atomic thermal motion has been modelled by extrapolating the ADPs of Hazen (1976). The topological analysis of the static electron density of periclase reveals, in the asymmetric unit, the presence of a 'bonding CP' [*i.e.* (3,-1); hereafter 'BCP'] along the Mg-O bond path at $(x, 0, 0)$ with $x \sim 0.22$, a BCP along the O-O direction at $(\frac{1}{4}, \frac{1}{4}, 0)$, a 'ring CP' [*i.e.* (3,+1); hereafter 'RCP'] along O-O at $(x, x, 0)$ with $x \sim 0.19$ and a 'cage CP' [*i.e.* (3,-3); hereafter 'CCP'] at $(\frac{1}{4}, \frac{1}{4}, \frac{1}{4})$. No evidence of catastrophe-related topological features has been found in the static electron density upon expanding the cell up to $a = 4.5$ Å, which nominally corresponds to $\simeq 4200$ K. Conversely, the analysis of the dynamic electron density sheds light on a catastrophe involving the (3,-1) CP lying on the O-O diagonal. Such a BCP tends to coalesce with an RCP along [110]. In Fig. 2 the temperature effect on $\rho(\mathbf{x})$ is shown, comparing the electron-density profiles along [110], at 300 and 3100 K. Fig. 3 displays as a function of T the degenerating eigenvalue of BCP, and we predict that at $T \simeq 3100$ K λ_2 becomes practically 0. Coalescence takes place through a closing in on the BCP at $(\frac{1}{4}, \frac{1}{4}, 0)$ of

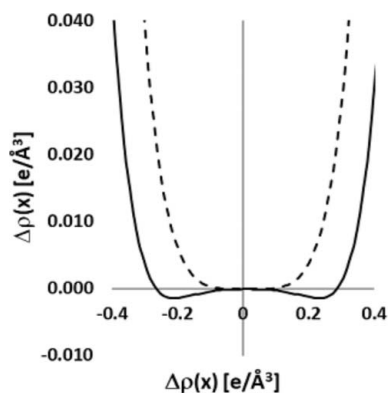


Figure 2
Dynamical $\Delta\rho(x)$ [*i.e.* $\rho(x) - \rho(x_{\text{critical}})$] versus Δx [*i.e.* $x - x_{\text{critical}}$] along the [110] direction in MgO periclase. Full and dashed lines correspond to 300 and 3100 K, respectively. Room pressure.

the symmetry-equivalent RCPs that are related to the (3,+1) CP at $(x, x, 0)$. In the end, a single RCP resulting from coalescence of BCP and RCPs occurs at $(\frac{1}{4}, \frac{1}{4}, 0)$, as shown in Fig. 4. The agreement between model and observation, in terms of temperature of the transformation of state, is $\simeq 3\%$. By way of example, we also calculated the integration critical radius, *i.e.* r_0 . Given that it is difficult to determine $\Phi(\Delta x_2)_{Xc}$, we have obtained it as a limit, *i.e.*

$$\lim_{X \rightarrow Xc} \Phi(\Delta x_2)_X,$$

where

$$\Phi(\Delta x_2)_X = \rho(\mathbf{x}_0 + \Delta) - \rho(\mathbf{x}_0) - \frac{1}{2}\lambda_2 \times \Delta x_2^2$$

and $\Delta = (0, \Delta x_2, 0)$. A series of X values has been sampled so as to have a monotonically decreasing $\lambda_2(X)$ trend. For every X value, we have analysed the related $\Phi(\Delta x_2)_X$ in terms of sixth-order polynomial expansions in Δx_2 . $\Phi(\Delta x_2)_{Xc}$, resulting from an extrapolation to Xc of the $\Phi(\Delta x_2)_X$ functions' coefficients, has allowed one to determine r_0 . In so doing, we have calculated an r_0 as large as about 0.10 Å.

Altogether, the melting of MgO at room pressure can be classified as a transformation of state compatible with an elementary Thom catastrophe of the cusp type, *i.e.* such that it converts a CP of a given parity (in our case the RCP) into two

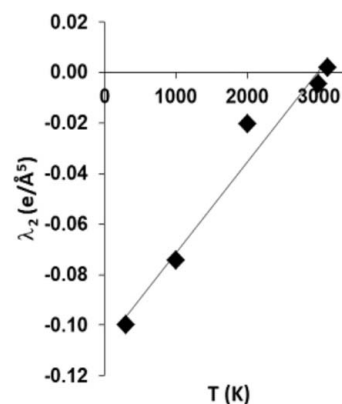


Figure 3
 λ_2 value of the (3,-1) CP along the O-O bond path for melting of MgO periclase at room pressure. At ~ 3100 K degeneracy takes place.

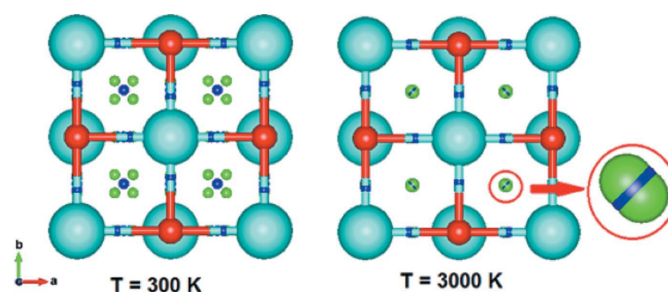


Figure 4
Room-pressure melting of MgO periclase. Projection onto (001) plane. Turquoise spheres = Mg atoms; red spheres = O atoms; small blue spheres = BCP; small green spheres = RCP; small yellow spheres = CCP; NCP at nuclear positions. BCPs and the RCPs involved in the transition are in a circle with a red rim.

CPs and *vice versa*, one of the same parity (RCP) and the other of opposite parity (BCP).

3.2. MgO B1–B2 phase transition at high *P/T* conditions

A MgO B1–B2 phase transition at high pressure and high temperature occurs above 400 GPa and ~ 9000 K (Coppari *et al.*, 2013; McWilliams *et al.*, 2012). To investigate such a case, we have to resort to the dynamic $\rho(\mathbf{x})$ obtained by ADPs from lattice dynamics. In so doing, we observe an O–O BCP at $(\frac{1}{4}, \frac{1}{4}, 0)$, comparatively close to an RCP at $(x, x, 0)$, $x \simeq 0.22$. Following a mechanism similar to that discussed in the previous section for periclase melting, the BCP coalesces with RCPs. The resulting topology is locally characterized by a single RCP, at $(x, x, 0)$, with $x = 1/4$ (Fig. 5). A BCP's eigenvalue tends to 0 upon T approaching a value that we have estimated of about 8650 K, at nominally 500 GPa. This behaviour is consistent with an elementary cusp-type catastrophe, *i.e.* similar to the case of MgO periclase melting, at room pressure. The agreement between prediction and experimental observation of the B1–B2 transition temperature is approximately $\simeq 4\%$. A precise determination of r_0 is difficult and time consuming; therefore, we limit our analysis to observe that $-V/U > 0$, for electron-density functions determined along the degenerating eigenvector of the BCP upon approaching the transition temperature.

3.3. TiO₂ rutile melting at room pressure

TiO₂ rutile is tetragonal (space group $P4_2/mnm$, $Z = 2$; Burdett *et al.*, 1987) with a Ti atom octahedrally coordinated by six O atoms, and melts at room pressure and $\simeq 2143$ K (Guisbiers *et al.*, 2008). We have used the lattice parameters extrapolated from the data of Meagher & Lager (1979) to model the rutile elementary cell at high temperature. Leaving aside any coherence between rutile stability as a periodic solid and high temperature, we have formally extrapolated experimental data even above 4000 K. The static electron density of rutile yields in the elementary cell six ‘nuclear CPs’ [*i.e.* (3, –3); hereafter ‘NCP’], 16 BCPs, 26 RCPs and 16 CCPs, over the interval $300 < T < 4000$ K. BCPs, RCPs and CCPs decrease to 12, 14 and 8, respectively, at higher temperatures. At

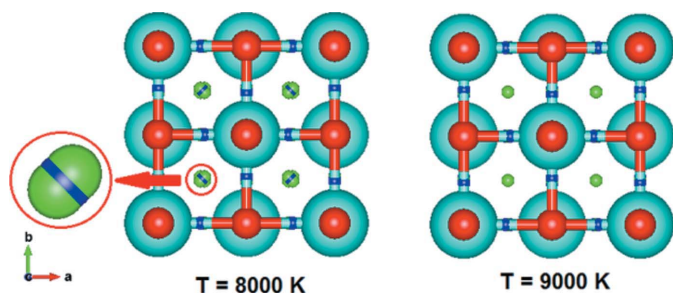


Figure 5 High-pressure and high-temperature transition of MgO periclase. Projection of MgO onto (001) plane. Turquoise spheres = Mg atoms; red spheres = O atoms; small blue spheres = BCP; small green spheres = RCP; small yellow spheres = CCP; NCP at nuclear positions. BCPs and RCPs involved in the transition are in a circle with a red rim.

$\simeq 4000$ K a BCP, sited at $(0, \frac{1}{2}, 0)$, becomes quasi-degenerate, exhibiting a $\lambda_1 = -0.0008 e \text{ \AA}^{-5}$. Such a BCP is close to an RCP at $(0.0091, 0.48467, 0)$, being $\simeq 0.086 \text{ \AA}$ apart. At $T \simeq 4500$ K, a BCP and RCP have coalesced into a quasi-degenerate RCP ($\lambda_1 = -0.00005 e \text{ \AA}^{-5}$). All this points to a transformation that is coherent with a cusp-type catastrophe. In the range $4000 < T < 4500$ K ($\simeq 4200$ K by interpolation, modelling T in 100 K intervals from 4000 to 4500 K) a negative eigenvalue of the BCP changes into a positive one, passing through a value of zero. In Fig. 6 the rutile structures and their CPs are shown, at 4000 and 4500 K, by way of example. Altogether, this proves that catastrophe-type conditions have occurred, but at temperatures far higher than the actual rutile melting point. In such a case, we have to resort to the dynamic electron density, obtained using an extrapolation of the ADPs from Meagher & Lager (1979). While modelling the topology of the static map yields an estimate of the melting temperature affected by an error of $\simeq 94\%$, the analysis of the dynamic electron density leads to a prediction in agreement with observation of $\simeq 5\%$. In Fig. 7, rutile structures and their CPs at $T = 2000$ K and $T = 2100$ K are displayed. Two CPs [BCP at $(0, \frac{1}{2}, 0)$ and an RCP at $(0.0292, 0.5509, 0)$] are very close to one another at 2000 K, whereas they have coalesced into one RCP at 2100 K. On the basis of simulations at 2020–2040–2060–2080 K, we predict a transition temperature $\simeq 2050$ K, in keeping with $-V/U > 0$, determined for $\rho(\mathbf{x})$ calculated along the direction of the eigenvector related to the degenerating BCP's eigenvalue. Note that both static and dynamic $\rho(\mathbf{x})$'s are able to predict conditions of instability and such loss of equilibrium can be ascribed to the same mechanism, but at quite different temperatures owing to the atomic thermal motion effects.

3.4. Al₂O₃ corundum: high-pressure phase transition to Rh₂O₃ (II)-type structure

Corundum crystallizes at ambient conditions with the space group $R\bar{3}c$, in which cations occupy a six-coordination posi-

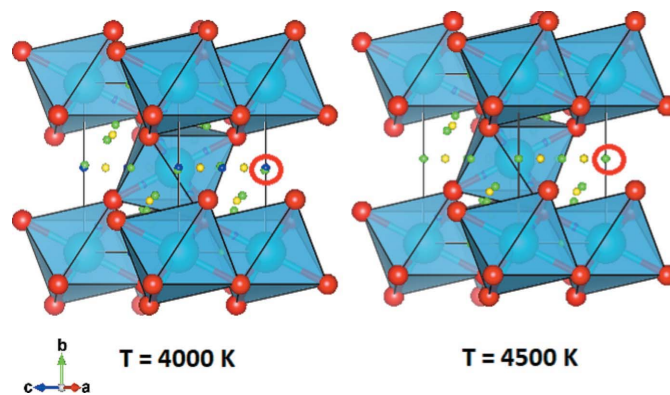
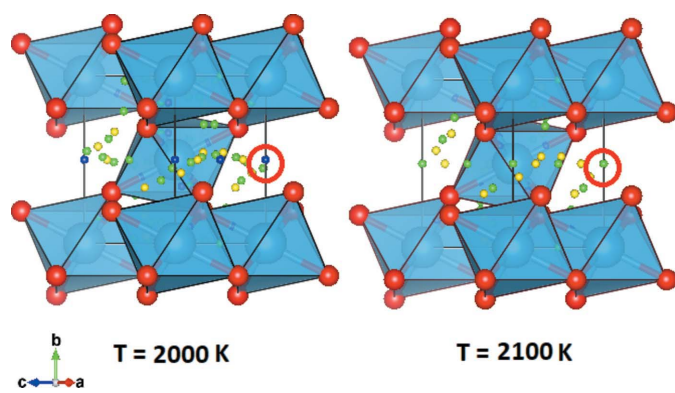
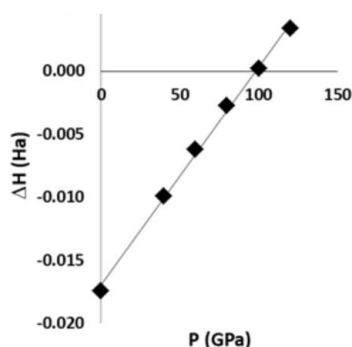


Figure 6 Room-pressure melting of TiO₂ rutile. Static electron density. Projection onto (101) plane at 4000 and 4500 K. Blue spheres, in transparency = Ti atoms; red spheres = O atoms; small blue spheres = BCP; small green spheres = RCP; small yellow spheres = CCP; NCP at nuclear positions. BCPs and RCPs involved in the transition are in a circle with a red rim.


Figure 7

Room-pressure melting of TiO_2 rutile. Dynamical electron density. Projection onto (101) plane at 2000 and 2100 K. Blue spheres, in transparency = Ti atoms; red spheres = O atoms; small blue spheres = BCP; small green spheres = RCP; small yellow spheres = CCP; NCP at nuclear positions. BCPs and RCPs involved in the transition are in a circle with a red rim.

tion. Upon increasing pressure, corundum changes into a Rh_2O_3 (II)-type structure, with space group $Pbcn$ (Marton & Cohen, 1994; Thomson *et al.*, 1996; Funamori, 1997; Mashimo *et al.*, 2000; Lin *et al.*, 2004; Kato *et al.*, 2013). Some theoretical studies also predict that Al_2O_3 can further pass into a perovskite-like structure, with space group $Pbnm$, at $P > 200$ GPa (Thomson *et al.*, 1996; Duan *et al.*, 1998). Oganov & Ono (2005) report CaIrO_3 -structure Al_2O_3 (post-perovskite structure) with space group $Cmcm$; such a phase is more stable at high pressures than perovskite structure (Caracas & Cohen, 2005; Tsuchiya *et al.*, 2004). Our simulations of corundum and Rh_2O_3 (II)-structure Al_2O_3 phases in static approximation show that the latter is stable up to 100 GPa, as can be seen in the enthalpy difference plot of Fig. 8. This is in agreement with the estimate of the transition pressure obtained by means of the analysis of the electron-density CPs. In corundum, static electron density yields 30 NCPs, 90 BCPs, 108 RCPs and 48 CCPs, in the range $0 < P < 95$ GPa. Looking at Fig. 9, it can be seen that at 95 GPa an RCP at $(0, \frac{1}{2}, 0)$ with $\lambda_1 = 0.009 \text{ e } \text{\AA}^{-5}$ occurs, while at 100 GPa such a CP disappears and is replaced by a BCP, with $\lambda_1 = -0.001 \text{ e } \text{\AA}^{-5}$, surrounded by two RCPs, 0.21 \AA away from it. This phenomenon is consistent with an elementary catastrophe of the cusp type. Using dynamic electron density (Fig. 10), obtained by ADPs from

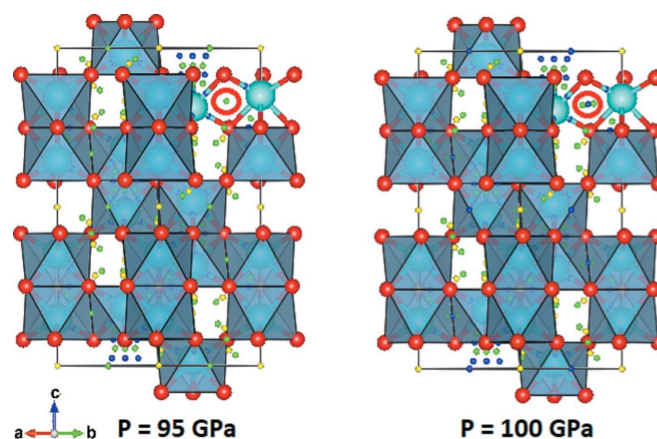

Figure 8

Al_2O_3 ; enthalpy difference between corundum and Rh_2O_3 (II) phase.

lattice dynamics, at $P = 105$ GPa and $1000 < T < 1900$ K, we have found the same CP behaviour as that observed in the static case. In particular, at 1000 K an RCP at $(\frac{1}{2}, 0, 0)$ with $\lambda_1 = 0.12 \text{ e } \text{\AA}^{-5}$ occurs, while at 1900 K it is substituted by a BCP, $\lambda_1 = -0.45 \text{ e } \text{\AA}^{-5}$, surrounded by two RCPs about 0.23 \AA away from it. The RCP-to-BCP conversion leads to an electron density that shows $-V/U > 0$ along the degenerating eigenvector. Interpolation of data calculated over the range 1000–1900 K and 90–110 GPa allows an estimate of the transition temperature of $\simeq 1900$ K and $\simeq 105$ GPa, which is in good agreement, some 1–2%, with the laser-heated diamond anvil cell experiments by Kato *et al.* (2013).

3.5. Earlier investigations: SiO_2 and $\text{Mg}_2\text{Si}_2\text{O}_6$

Merli & Sciascia (2013) and Merli *et al.* (2011) correlate the appearance of degenerate CPs to the occurrence of phase transitions at high pressure, for SiO_2 α -quartz \rightarrow coesite, and at high temperature, for $\text{Mg}_2\text{Si}_2\text{O}_6$ $Pbca$ (enstatite) \rightarrow $Pbcn$ (enstatite). In both cases, fold-type catastrophes take place, *i.e.* two CPs of different signatures coalesce into a non-critical point, a ‘wandering point’ as stated above. In particular, an RCP and BCP are involved for both SiO_2 and $\text{Mg}_2\text{Si}_2\text{O}_6$. In the case of SiO_2 , the predicted pressure is about 4 GPa, some 25% larger than the observed one. It is possible for such a discrepancy to be ascribable to the comparatively low pressure of transition, which is highly sensitive to temperature, as shown by Bose & Ganguly (1995), and for its P value of occurrence to change accordingly. The $\text{Mg}_2\text{Si}_2\text{O}_6$ transition is located between 1300 and 1400 K, in good agreement with its observed occurrence at some 1360 K. In such a case, Merli *et al.* (2011) did not resort to the use of dynamic electron density. This might be ascribed to the $Pbca \rightarrow Pbcn$ transition being a low-energy transition involving breaking of an O–O bond, and it does not imply such large cation vibrations as those that conversely occur in transformations of state from solid to melt.


Figure 9

Static electron density. Projection of Al_2O_3 corundum onto the (110) plane. Blue spheres, in transparency = Al atoms; red spheres = O atoms; small blue spheres = BCP; small green spheres = RCP; small yellow spheres = CCP; NCP at nuclear positions. BCPs and RCPs involved in the transition are in a circle with a red rim.

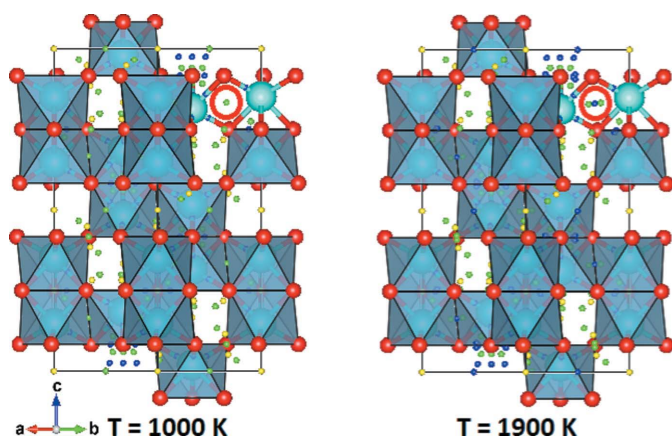


Figure 10

Dynamic electron density at $P = 105$ GPa. Projection of Al_2O_3 corundum onto the (110) plane. Blue spheres, in transparency = Al atoms; red spheres = O atoms; small blue spheres = BCP; small green spheres = RCP; small yellow spheres = CCP; NCP at nuclear positions. BCPs and RCPs involved in the transition are in a circle with a red rim.

4. Conclusions

The impressive advances achieved in reconstructing electron density from diffraction experiments at non-ambient conditions motivate us to pay special attention to $\rho(\mathbf{x})$ as an observable parameter whose topology can carry information about stability/instability of a crystal phase. The combination of electron-density critical points analysis and catastrophe theory provides a way to predict instability occurrence triggered, in the cases explored here, by pressure and/or temperature. In particular, the annihilation of one eigenvalue of the Hessian matrix at a CP, *i.e.* occurrence of degeneracy, hints at possible phase/state transformations. All this is viewed in the light of the Thom catastrophe theory, on the one hand, and it is energetically accounted for through the notion of ‘integration critical radius’, r_0 , that is introduced here. On the other hand, r_0 represents the size of the integration region around a degenerate CP at given P – T , such that the Gibbs energy of the related periodic solid is an expansion in r_0 with features that in the catastrophe formalism are associated with a rise in instability [see equation (7a)]. Coalescing of CPs into a CP of different signature, or into a ‘wandering point’, implies occurrence of degeneracy. We have determined electron density by enthalpy minimization at non-ambient conditions using a hybrid HF–DFT approach, which exploits linear combination of atomic orbitals. A difficulty arises from the fact that static $\rho(\mathbf{x})$ may be insufficient to bring to light instability, or leads to large errors in predicting P – T values of transformation (see Table 1), in particular at room pressure and very high temperature regimes. Dynamic electron density is to be used in place of the static one to overcome such problems. Making $\rho(\mathbf{x})$ dynamic is here performed *via* introduction of atomic displacement parameters. ADPs, in turn, are determined either by lattice dynamics or by an extrapolation to high temperature of experimental values. This second course has been followed in the case of room-pressure and high-temperature transformations. Dynamic $\rho(\mathbf{x})$ is then

retrieved through the maximum entropy method, using dynamic Fourier coefficients up to $|\mathbf{H}| \simeq 18 \text{ \AA}^{-1}$. We have studied the phase/state transitions in the case of three simple oxides: MgO periclase, TiO_2 rutile and Al_2O_3 corundum. The agreement between predicted transition/transformation pressure/temperature and the observed one ranges between 3 and 5%. Notwithstanding the satisfactory agreement between observations and forecasts, we are more interested in the general transferability of the theoretical approach to periodic solid transformations, than to the precision of the present results, which anyway seem to positively point to a methodological validity. From such a viewpoint, one may expect advances and enhancements in the future with regard to the ability to account for and introduce thermal dependence in the static electron density. Moreover, other sources of uncertainty are zero-point contribution and thermal contribution to P , which have been neglected here in estimating pressure.

Altogether, we believe the electron-density CP degeneration may be related to instability occurrence in crystals, at high-pressure/temperature conditions. Although such a general principle holds for the case studies discussed here, the practical use of $\rho(\mathbf{x})$ CPs to unearth and predict transformations is still in need of enhancements to overcome the difficulties mentioned above, and more investigations are required to shed light on the univocal relation between ‘CP degeneration’ and loss of stability.

Acknowledgements

A. Pavese is grateful to the Earth Sciences Department ‘Ardito Desio’ (University of Milan) for the support provided to carry out this research (which started in 2013). The authors are thankful to the editor and two anonymous referees for suggestions and corrections, which improved the quality of the original manuscript.

References

- Andrés, J., Gracia, L., González-Navarrete, P. & Safont, V. S. (2015). *Comput. Theor. Chem.* **1053**, 17–30.
- Arnol’d, V. L. (1986). *Catastrophe Theory*, 2nd ed. Berlin: Springer Verlag.
- Bader, R. (1990). *Atoms in Molecules: a Quantum Theory*. USA: Oxford University Press.
- Boldyreva, E. & Dera, P. (2009). *High Pressure Crystallography: From Fundamental Phenomena to Technological Applications*. The NATO Science for Peace and Security Series. Berlin: Springer Verlag.
- Bose, K. & Ganguly, J. (1995). *Am. Mineral.* **80**, 231–238.
- Bredow, T., Heitjans, P. & Wilkening, M. (2004). *Phys. Rev. B*, **70**, 115111.
- Burdett, J. K., Hughbanks, T., Miller, G. J., Richardson, J. W. Jr & Smith, J. V. (1987). *J. Am. Chem. Soc.* **109**, 3639–3646.
- Caracas, R. & Cohen, R. E. (2005). *Geophys. Res. Lett.* **32**, L06303.
- Casati, N., Genoni, A., Meyer, B., Krawczuk, A. & Macchi, P. (2017). *Acta Cryst.* **B73**, 584–597.
- Casati, N., Kleppe, A., Jephcoat, A. & Macchi, P. (2016). *Nat. Commun.* **7**, 10901.
- Catti, M. (2002). *Phys. Rev. B*, **65**, 224115–224122.
- Catti, M. (2005). *Phys. Rev. B*, **72**, 064105–064111.

- Causà, M., Dovesi, R., Pisani, C. & Roetti, C. (1986). *Phys. Rev. B*, **33**, 1308–1316.
- Contreras-García, J., Martín Pendás, Á. M., Silvi, B. & Manuel Recio, J. (2008). *J. Phys. Chem. Solids*, **69**, 2204–2207.
- Contreras-García, J., Martín Pendás, A. & Recio, J. M. (2008). *J. Phys. Chem. B*, **112**, 9787–9794.
- Coppari, F., Smith, R. F., Eggert, J. H., Wang, J., Rygg, J. R., Lazicki, A., Hawreliak, J. A., Collins, G. W. & Duffy, T. S. (2013). *Nat. Geosci.* **6**, 926–929.
- Dittrich, B. (2017). *Acta Cryst.* **B73**, 325–329.
- Dovesi, R., Saunders, V. R., Roetti, C., Orlando, R., Zicovich-Wilson, C. M., Pascale, F., Civalleri, B., Doll, K., Harrison, N. M., Bush, I. J., D'Arco, P. & Llunell, M. (2009). *CRYSTAL09 User's Manual*. University of Torino, Italy.
- Duan, W., Paiva, G., Wentzcovitch, R. M. & Fazzio, A. (1998). *Phys. Rev. Lett.* **81**, 3267–3270.
- Dubrovinsky, L. S. & Saxena, S. K. (1997). *Phys. Chem. Miner.* **24**, 547–550.
- Fabbiani, F. P. A., Dittrich, B., Pulham, C. R. & Warren, J. E. (2011). *Acta Cryst.* **A67**, C376.
- Flurry, P. A. (1976). *Annu. Rev. Mater. Sci.* **6**, 157–180.
- Funamori, N. (1997). *Science*, **278**, 1109–1111.
- Gatti, C. & Casassa, S. (2014). *TOPOND User's Manual*. CNR-ISTM of Milano, Italy.
- Gatti, C., Saunders, V. R. & Roetti, C. (1994). *J. Chem. Phys.* **101**, 10686–10696.
- Ghose, S., Coey, J. M. D. & Salje, E. (2012). *Structural and Magnetic Phase Transitions in Minerals. Advances in Physical Geochemistry*. Berlin: Springer Verlag.
- Gilmore, R. (1993). *Catastrophe Theory for Scientists and Engineers*. New York: Dover.
- Guisbiers, G., Van Overschelde, O. & Wautelet, M. (2008). *Appl. Phys. Lett.* **92**, 103121.
- Hazen, R. M. (1976). *Am. Miner.* **61**, 266–271.
- Hemley, R. J. (1998). In *Ultrahigh Pressure Mineralogy: Physics and Chemistry of the Earth's Deep Interior. Reviews in Mineralogy*, Vol. 37. Mineralogical Society of America.
- Kato, J., Hirose, K., Ozawa, H. & Ohishi, Y. (2013). *Am. Mineral.* **98**, 335–339.
- Lin, J. F., Degtyareva, O., Prewitt, C., Dera, P., Sata, N., Gregoryanz, E., Mao, H. & Hemley, R. J. (2004). *Nat. Mater.* **3**, 389–393.
- Luaña, V., Costales, A. & Martín Pendás, A. (1997). *Phys. Rev. B*, **55**, 4285–4297.
- Macchi, P. (2017). *Acta Cryst.* **B73**, 330–336.
- Macchi, P. & Casati, N. (2011). *Acta Cryst.* **A67**, C163–C164.
- Martín Pendás, A., Costales, A. & Luaña, V. (1997). *Phys. Rev. B*, **55**, 4275–4284.
- Marton, F. C. & Cohen, R. E. (1994). *Am. Mineral.* **79**, 789–792.
- Mashimo, T., Tsumoto, K., Nakamura, K., Noguchi, Y., Fukuoka, K. & Syono, Y. (2000). *Geophys. Res. Lett.* **27**, 2021–2024.
- Matta, C. F. & Boyd, R. J. (2007). *The Quantum Theory of Atoms in Molecules*. Weinheim: Wiley-VCH Verlag GmbH and Co. KGaA.
- McWilliams, R. S., Spaulding, D. K., Eggert, J. H., Celliers, P. M., Hicks, D. G., Smith, R. F., Collins, G. W. & Jeanloz, R. (2012). *Science*, **338**, 1330–1333.
- Meagher, E. P. & Lager, G. A. (1979). *Can. Mineral.* **17**, 77–85.
- Merli, M., Nestola, F. & Sciascia, L. (2011). *Eur. J. Mineral.* **23**, 197–205.
- Merli, M. & Pavese, A. (2006). *Z. Kristallogr.* **221**, 613–620.
- Merli, M., Pavese, A. & Curetti, N. (2009). *Phys. Chem. Miner.* **36**, 19–28.
- Merli, M., Pavese, A. & Ranzini, M. (2002). *Phys. Chem. Miner.* **29**, 455–464.
- Merli, M. & Sciascia, L. (2013). *Phys. Chem. Miner.* **40**, 455–466.
- Milettinger, R. (2005). Editor. *EMU Notes: Mineral Behaviour at Extreme Conditions*, Vol. 7. European Mineralogical Union.
- Montanari, B., Civalleri, B., Zicovich-Wilson, C. M. & Dovesi, R. (2006). *Int. J. Quantum Chem.* **106**, 1703–1714.
- Oganov, A. R. & Ono, S. (2005). *Proc. Natl Acad. Sci. USA*, **102**, 10828–10831.
- Otero-de-la-Roza, A., Blanco, M. A., Martín Pendás, A., & Luaña, V. (2009). *Comput. Phys. Commun.*, **180**, 157–166.
- Otero-de-la-Roza, A., Johnson, E. R. & Luaña, V. (2014). *Comput. Phys. Commun.* **185**, 1007–1018.
- Parisi, F., Sciascia, L., Princivalle, F. & Merli, M. (2012). *Phys. Chem. Miner.* **39**, 103–113.
- Peintinger, M. F., Vilela Oliveira, D. & Bredow, T. (2013). *J. Comput. Chem.* **34**, 451–459.
- Reeber, R. R., Goessel, K. & Wang, K. (1995). *Eur. J. Mineral.* **7**, 1039–1048.
- Sanns, W. (2009). *Encyclopedia of Complexity and System Science*, edited by R. A. Meyers, pp. 703–719. Larkspur, California: Springer Verlag.
- Scanavino, I., Belousov, R. & Prencipe, M. (2012). *Phys. Chem. Miner.* **39**, 649–663.
- Scott, J. F. (1974). *Rev. Mod. Phys.* **46**, 83–128.
- Smaalen, S. van, Palatinus, L. & Schneider, M. (2003). *Acta Cryst.* **A59**, 459–469.
- Thom, R. (1975). *Structural Stability and Morphogenesis*. Reading, Massachusetts: W. A. Benjamin.
- Thomson, K. T., Wentzcovitch, R. M. & Bukowinski, M. S. T. (1996). *Science*, **274**, 1880–1882.
- Tse, J. S., Klug, D. D., Patchkovskii, S., Ma, Y. & Dewhurst, J. K. (2006). *J. Phys. Chem. B*, **110**, 3721–3726.
- Tsuchiya, T., Tsuchiya, J., Umamoto, K. & Wentzcovitch, R. M. (2004). *Earth Planet. Sci. Lett.* **224**, 241–248.
- Wu, Z. & Cohen, R. E. (2006). *Phys. Rev. B*, **73**, 235116–235121.
- Yamanaka, T., Okada, T. & Nakamoto, Y. (2009). *Phys. Rev. B*, **80**, 094108.